

# Suppression of vortex shedding behind a circular cylinder by another control cylinder at low Reynolds numbers

By A. DIPANKAR, T. K. SENGUPTA AND S. B. TALLA

Department of Aerospace Engineering, IIT Kanpur 208 016, India

(Received 12 September 2004 and in revised form 15 August 2006)

Vortex shedding behind a cylinder can be controlled by placing another small cylinder behind it, at low Reynolds numbers. This has been demonstrated experimentally by Strykowski & Sreenivasan (*J. Fluid Mech.* vol. 218, 1990, p. 74). These authors also provided preliminary numerical results, modelling the control cylinder by the innovative application of boundary conditions on some selective nodes. There are no other computational and theoretical studies that have explored the physical mechanism. In the present work, using an over-set grid method, we report and verify numerically the experimental results for flow past a pair of cylinders. Apart from providing an accurate solution of the Navier–Stokes equation, we also employ an energy-based receptivity analysis method to discuss some aspects of the physical mechanism behind vortex shedding and its control. These results are compared with the flow picture developed using a dynamical system approach based on the proper orthogonal decomposition (POD) technique.

---

## 1. Introduction

Vortex shedding behind a circular cylinder at low Reynolds numbers has been altered by the placement of a smaller cylinder in the near wake of the cylinder (Strykowski 1986; Strykowski & Sreenivasan 1990). Hereinafter, the bigger cylinder will be referred to as the main cylinder, whereas the smaller cylinder in the wake of the main cylinder will be referred to as the control cylinder. From experimental observations, the authors concluded that the control cylinder (i) reduces the temporal growth rate of disturbances; (ii) alters or controls vortex shedding that shows up in reduced drag and movement of peaks at lower frequencies in the spectrum; (iii) changes the local stability by smearing and diffusing concentrated vorticity by diverting a small amount of fluid in the near-wake of the main cylinder. Vortex shedding was suppressed for Reynolds numbers ( $Re$ , defined by the diameter  $D$  of the main cylinder and the oncoming free-stream speed) below 80. They also reported numerical results for  $Re = 55$  in a small physical domain ( $-3.4 < x/D < 9.7$ ) using a second-order finite-difference Galerkin method. The problem was solved using a single block-structured grid and the control cylinder was modelled by enforcing a no-slip condition on six grid points occupying an area similar to that of the control cylinder.

Barring the early numerical results of Strykowski & Sreenivasan (1990), there are no other numerical efforts that reproduce the experimental observations of Strykowski (1986) and Strykowski & Sreenivasan (1990). First and foremost, to study this flow one needs accurate numerical methods that are free of spurious numerical dispersion effects, because, such spurious numerical dispersion leads to vortex shedding. Thus, it is

not easy to compute flows where such alternate shedding of vortices are suppressed or stopped physically. Lower-accuracy methods apart from being spuriously dispersive, also have larger truncation errors that trigger flow asymmetry and vortex shedding. In contrast, higher-order methods display delayed onset of flow asymmetry (see Nair & Sengupta 1996) owing to a lower level of asymmetric-error and numerical dispersion effects. Thus, satisfaction of physical dispersion relation (also termed the dispersion relation preservation (DRP) property) is central to computing physically unstable flows. Issues of accuracy, DRP property and numerical stability for direct simulation of transitional and turbulent flows are discussed in Sengupta (2004) – that and Sengupta, Ganeriwal & De (2003*b*) introduced some high-accuracy compact schemes which satisfy the above requirements of direct simulation. Secondly, it is difficult to produce an accurate solution for physically unstable flows in multiply-connected domains using structured non-orthogonal grids. The non-orthogonality requires the discretization of a larger number of terms, invariably introducing additional large sources of error. Solving the Navier–Stokes equation for this class of problems, by finite-element and finite-volume methods (FEM and FVM) using unstructured grids for multiply-connected domains will also not be successful, if adopted methods do not satisfy the DRP property. These shortcomings of many numerical schemes employed in commonly used FEM and FVM are discussed in Sengupta (2004) and Sengupta, Talla & Pradhan (2005) and other references contained therein. In the present work, the high-resolution compact scheme of Sengupta *et al.* (2003*b*) is used to solve Navier–Stokes equations on over-set orthogonal grids. The requirements for direct simulation of physically unstable flows are discussed in the Appendix (available with the online version of the paper), comparing the present finite-difference method with other popular spatial discretization methods used in finite-element and finite-volume calculations and the role of the correct far-field boundary condition.

The power of the emerging direct simulation methodologies has not been successfully translated as yet in computing physically unstable flows in a multiply-connected domain. Although, significant progress has been made in solving engineering problems using finite-element, finite-volume and finite-difference methods employing over-set grids for complex geometries. Developments in over-set grid method are given in Stegger & Benek (1987), Chesshire & Henshaw (1990) and Henshaw (1994). Extension of high-accuracy methods in conjunction with an over-set grid method is used here in solving the problem of the control of vortex shedding.

Strykowski & Sreenivasan (1990), Strykowski (1986) and Sreenivasan, Strykowski & Olinger (1987), identified vortex shedding as a result of absolute instability in the near-wake owing to the temporal growth of unstable modes. Jackson (1987) identified Hopf bifurcation of steady flow as producing periodic flows. In contrast, Sengupta *et al.* (2003*b*) have proposed vortex shedding as a consequence of spatio-temporal instability of an equilibrium solution. This equilibrium solution can represent either a steady or an unsteady primary flow. Theoretical explanation of the instability is based upon the time evolution of disturbance energy ( $E_d$ ), whose instantaneous spatial distribution is governed by an equation derived from the rotational form of the Navier–Stokes equation without making any simplifying assumption, as given in Sengupta, De & Sarkar (2003*a*),

$$\nabla^2 E_d = 2\boldsymbol{\omega}_m \cdot \boldsymbol{\omega}_d + \boldsymbol{\omega}_d \cdot \boldsymbol{\omega}_d - \mathbf{V}_m \cdot \nabla \times \boldsymbol{\omega}_d - \mathbf{V}_d \cdot \nabla \times \boldsymbol{\omega}_m - \mathbf{V}_d \cdot \nabla \times \boldsymbol{\omega}_d. \quad (1.1)$$

In this equation,  $\mathbf{V}$  and  $\boldsymbol{\omega}$  represent velocity and vorticity fields, respectively. The subscripts  $m$  and  $d$  refer to the equilibrium and the disturbance quantities. At any instant, one can solve the above Poisson equation to obtain the distribution of  $E_d$  from

the obtained solution of the Navier–Stokes equation. This approach was found most suitable in predicting bypass transition in Sengupta *et al.* (2003a) and Sengupta & Dipankar (2005), where growth or decay of  $E_d$  with time was predicted – not by solving equation (1.1) over successive time steps, but by looking at the presence of disturbance energy sources (sinks) given by the right-hand side of (1.1) where it becomes negative (positive). This mechanism of predicting growth and decay of disturbance energy is significant, as it is based on the full Navier–Stokes equation without any assumptions – unlike in other instability theories.

Vortex shedding behind a bluff body displays complicated spatio-temporal variations that can be analysed using proper orthogonal decomposition (POD) as a tool. POD as a statistical technique allows us to present coherent structures as a low-dimensional description of the flow. Also, POD as a linear operation allows us to study the flow locally that can be used to discriminate between pockets of convective and absolute instability for bluff-body flows. Deane & Mavriplis (1994) and Deane *et al.* (1991) have used the POD technique to propose vortex shedding as being due to interactions between the leading pair of eigen-modes that are roughly  $90^\circ$  phase apart in time and this, coupled with the discrepancy in phase in space (streamwise direction), leads to the travelling character of the vortex street. The higher modes represent higher frequencies and also possess travelling character as the leading pair.

In the present study, we have tried to interpret vortex shedding and its suppression in terms of unsteady disturbance energy growth, as given by (1.1), and in terms of POD modes. In the next section, the numerical simulation methods and results are given for a few specific cases studied. In §3, vortex shedding is viewed in terms of unsteady disturbance growth. This is followed by the characterizing of vortex shedding and its control by POD in §4. The paper closes with a summary of the present work.

## 2. Numerical simulation of vortex-shedding and suppression cases

In the present computations, the Navier–Stokes equation is solved using streamfunction–vorticity ( $\psi - \omega$ ) formulation. Governing equations are solved using the over-set grids shown in figure 1(a). Details of basic numerical methods used for solving the vorticity transport equation are as given in the online Appendix. We have considered two diameter ratio cases for the main ( $D$ ) and control cylinders ( $d$ ); Case A:  $D/d = 7$  for  $Re = 150$  and Case B:  $D/d = 10$  for  $Re = 63$  and  $79$ . Some experimental results for these cases are given in Strykowski (1986) and Strykowski & Sreenivasan (1990) and are used here to validate the computations. For Case A, the control cylinder is positioned at  $x/D = 1.75$  and  $y/D = 1$  with respect to the centre of the main cylinder. For Case B, the control cylinder is positioned at  $x/D = 1.2$  and  $y/D = 0.95$  with respect to the centre of the main cylinder. The outer boundary for the grid system,  $\Omega_1$ , for both the cases, extended up to  $40D$  with 301 equi-angularly spaced points in the azimuthal direction and 400 points in the wall-normal direction. The wall resolution of the radial grid line is  $0.005D$  for all the cases reported here. For Case A, the grid system around the control cylinder,  $\Omega_2$ , uses 201 points in the azimuthal direction and 80 points in the wall-normal direction, up to  $x = D$  from the centre of the control cylinder. For Case B, the grid system around the control cylinder,  $\Omega_2$ , uses 151 points in the azimuthal direction and 60 points in the radial direction, up to  $x = 0.65D$  from the centre of the control cylinder. Typical grid layout for the over-set method is shown in figure 1(a).

All the lower-Reynolds-number cases display alteration or suppression of shedding of vortices in the near wake, whereas the  $Re = 150$  case displays regular periodic shed

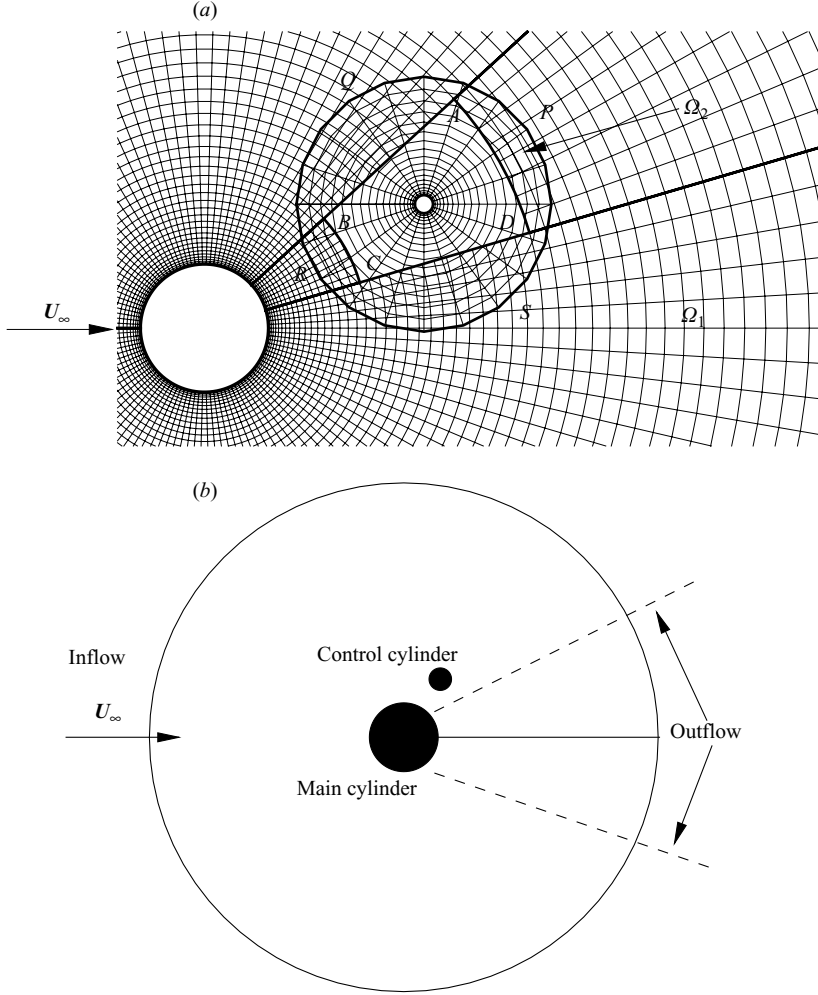


FIGURE 1. (a) Over-set grid shown using only limited grid lines and (b) schematic of the flow field identifying the inflow and outflow of the computing domain.

vortices in the wake. No data were reported for  $Re$  exceeding 120 in Strykowski (1986) and the results presented here for  $Re = 150$  are to show that the flow is controlled minimally, whereas it is effective at Reynolds number below 80. Here, the vorticity transport equation and the streamfunction equation that have been solved are given by,

$$\frac{\partial \omega}{\partial t} + (\mathbf{V} \cdot \nabla) \omega = \frac{1}{Re} \nabla^2 \omega, \quad (2.1)$$

$$\nabla^2 \psi = -\omega. \quad (2.2)$$

The non-dimensionalized equations have been obtained with  $D$  as the length scale and  $U_\infty$  as the velocity scale. Details of the inflow and outflow used for the grid system  $\Omega_1$  are shown in figure 1(b) for the purpose of applying boundary conditions. Equations (2.1) and (2.2) are solved subject to the no-slip boundary condition on the cylinder walls and uniform flow on the inflow of  $\Omega_1$ . At the outflow boundary

of  $\Omega_1$ , a convective boundary condition is used for the radial component of the velocity ( $V_r$ ):  $\partial V_r / \partial t + V_c \partial V_r / \partial r = 0$ , where  $V_c$  is the convection speed calculated from the previous time step at the outflow for  $V_r$ . This is based on the work reported in Esposito, Verzicco & Orlandi (1993) and Orlanski (1976), that addressed this important issue of the outflow boundary condition in correctly capturing flow past bluff bodies. Having obtained the  $V_r$ , we can calculate the streamfunction directly upon integration. Thereafter, vorticity is calculated from (2.2). This convective boundary condition (CBC) allows smooth passage of vortices through the outflow without any reflections. This outflow boundary condition is absolutely essential for the success of the present computations and additional discussion and results are provided in figure 13 of the online Appendix.

Here, (2.1) and (2.2) are solved in each of the sub-domains ( $\Omega_1, \Omega_2$ ) independently using synthesized boundary conditions obtained at the sub-domain boundaries, as defined in the following. To solve the problem in  $\Omega_1$ , auxiliary boundary conditions are obtained on  $ABCD$  of figure 1(a) from the solution obtained in  $\Omega_2$ . Similarly, to solve the problem in  $\Omega_2$ , auxiliary boundary conditions are required on  $PQRS$  that are supplied from the solution in  $\Omega_1$ . At each time step, this procedure is iterated until the solutions for (2.2) converge to the desired tolerance. The success of the over-set grid method depends on how accurately these auxiliary boundary conditions can be obtained at the inter-grid boundaries ( $ABCD$  and  $PQRS$  in figure 1a) from the donor neighbouring grids. The basic procedure followed in interpolating boundary data at an acceptor point ( $p$ ) is to consider a cloud of donor points in its neighbourhood. The interpolation of functions at this cloud of points in terms of the function and its derivatives at  $p$  gives the residue at the  $i$ th point as,

$$R_i = -f_i + f_p + f_x|_p \Delta x_i + f_y|_p \Delta y_i + f_{xx}|_p \frac{\Delta x_i^2}{2} + f_{yy}|_p \frac{\Delta y_i^2}{2} + f_{xy}|_p \Delta x_i \Delta y_i + \dots$$

We can construct an objective function,  $F = \sum_{i=1}^N R_i^2$ , and minimize it with respect to  $f_p$  and the derivatives  $f_x|_p, f_y|_p$ , etc. This shows that we require a minimum of three donor points for linear interpolation and six donor points for quadratic interpolation. Although more donor points can be used in a least-squares sense, it is noted that the accuracy is degraded when a larger number of donor points are used. In the present work, we have used a cloud of seven donor points for least-squares quadratic interpolation to obtain all the inter-grid boundary data.

Loads are calculated for the main cylinder by solving the pressure Poisson equation (PPE):

$$\nabla^2 \left( \frac{p}{\rho} + \frac{V^2}{2} \right) = \nabla \cdot (\mathbf{V} \times \boldsymbol{\omega}). \quad (2.3)$$

The quantity in the parentheses on the left-hand side is the total pressure and is a good measure of total mechanical energy for incompressible flows. Instead of solving this PPE in the multiply connected domain, here (2.3) is solved in a small part of  $\Omega_1$  surrounding the main cylinder. This is feasible, as the solution of the PPE can be performed as and when necessary, using the velocity and vorticity information in the domain. Furthermore, we can obtain very accurate boundary conditions derived from the normal momentum equation as applied to the solid body in  $\Omega_1$  and to the outer boundary used for solving the PPE:

$$\frac{h_1}{h_2} \frac{\partial p}{\partial \eta} = -h_1 u \omega + \frac{1}{Re} \frac{\partial \omega}{\partial \xi} - h_1 \frac{\partial v}{\partial t}, \quad (2.4)$$

where  $\xi$  and  $\eta$  are the contra-variant azimuthal and radial transformed coordinates and  $h_1 = (x_\xi^2 + y_\xi^2)^{1/2}$  and  $h_2 = (x_\eta^2 + y_\eta^2)^{1/2}$  are the scale factors of transformation from the Cartesian to  $(\xi, \eta)$ -coordinate system;  $u$  and  $v$  are the azimuthal and radial contra-variant components of velocity. In (2.4), all the quantities on the right-hand side can be accurately evaluated from the solution of (2.1) and (2.2). These boundary conditions are ‘exact’ if the derivatives in the normal momentum equation are calculated accurately enough. Because of this, we can truncate  $\Omega_1$  for solving PPE and obtain loads for different parts of a multiply-connected domain separately. Details of the rationale and procedures for solving the PPE in a truncated domain are given in Sengupta, Vikas & Johri (2006). In the present exercise, the first 50 radial lines have been used in the truncated  $\Omega_1$  domain to solve the PPE. The obtained pressure and vorticity fields are integrated to calculate loads acting on the main cylinder. This particular method of fixing the Neumann boundary condition at the outflow, at a small distance from the main cylinder shows unsteadiness in the calculated loads, i.e. the unsteady boundary conditions cause unsteadiness in the calculated pressure at high frequencies.

Results for lift and drag coefficients are shown for all the computed cases in figures 2. For Case A ( $Re = 150$ ;  $D/d = 7$ ), results are shown for the controlled and uncontrolled cases in figure 2(a). There are small-scale variations in the calculated loads owing to the method of calculating the pressure field, as explained above. Additionally, conjugate gradient methods displays non-smooth residue variations in general and that can add to this. In this figure, the plots of  $C_l$  and  $C_d$  show the significant effects of the transient up to  $t = 20$  for the uncontrolled case. The periodic variations are clearly visible for the uncontrolled case, whereas for the controlled case, periodic variations are seen for  $C_l$ , with lower amplitude and longer time period. As shown in Nair & Sengupta (1996), the onset of asymmetry and vortex shedding for flow past a circular cylinder in computations depends on the accuracy of the numerical method, if the flow field does not have any preferred direction. In this case, fixing an outflow boundary (figure 1b) imposes a directionality and thus the onset of asymmetry is immediate at the impulsive start. It is also noted that there is a non-negligible drag reduction when the flow is controlled.

For the case of  $Re = 63$  ( $D/d = 10$ ), corresponding results for  $C_l$  and  $C_d$  are shown in figure 2(b). For this case, the effects of transients are seen for even smaller time duration and the positioning of the control cylinder significantly alters the shedding pattern. There are no visible periodic variations for  $C_l$  and  $C_d$  for this case. However, it is seen from the streamline contours that the vortex shedding takes place at location farther downstream, that does not affect the lift and drag coefficients. Strykowski (1986) found that the vortex shedding could be suppressed for up to  $Re = 80$ , so we have computed the case for  $Re = 79$  (figure 2c). In figure 2, the controlled flow is compared with the corresponding uncontrolled flow, which clearly shows the effect of control. Comparing this case with the case of  $Re = 150$ , we note a significantly higher drag reduction, as well as larger unsteadiness control in terms of amplitude and time period. The effects of lowering the Reynolds number is also clearly evident (figure 2).

To use the present calculations, it is necessary to check the validity of these results by comparing them with the experimental data in Strykowski (1986). We compare the Roshko number,  $F_R = f D^2 / \nu$ , which can be written in terms of the non-dimensional quantities used in the present computations as  $F_R = Re / T_p$ , where  $T_p$  is the time period of vortex shedding. In our calculations, we note the time period from the velocity history at  $x/D = 10$ . For the controlled case of  $Re = 79$  we note  $T_p = 8.08$ , and  $F_R = 9.77$ , which compares well with  $F_R \cong 9.0$  given in figure 24 of Strykowski

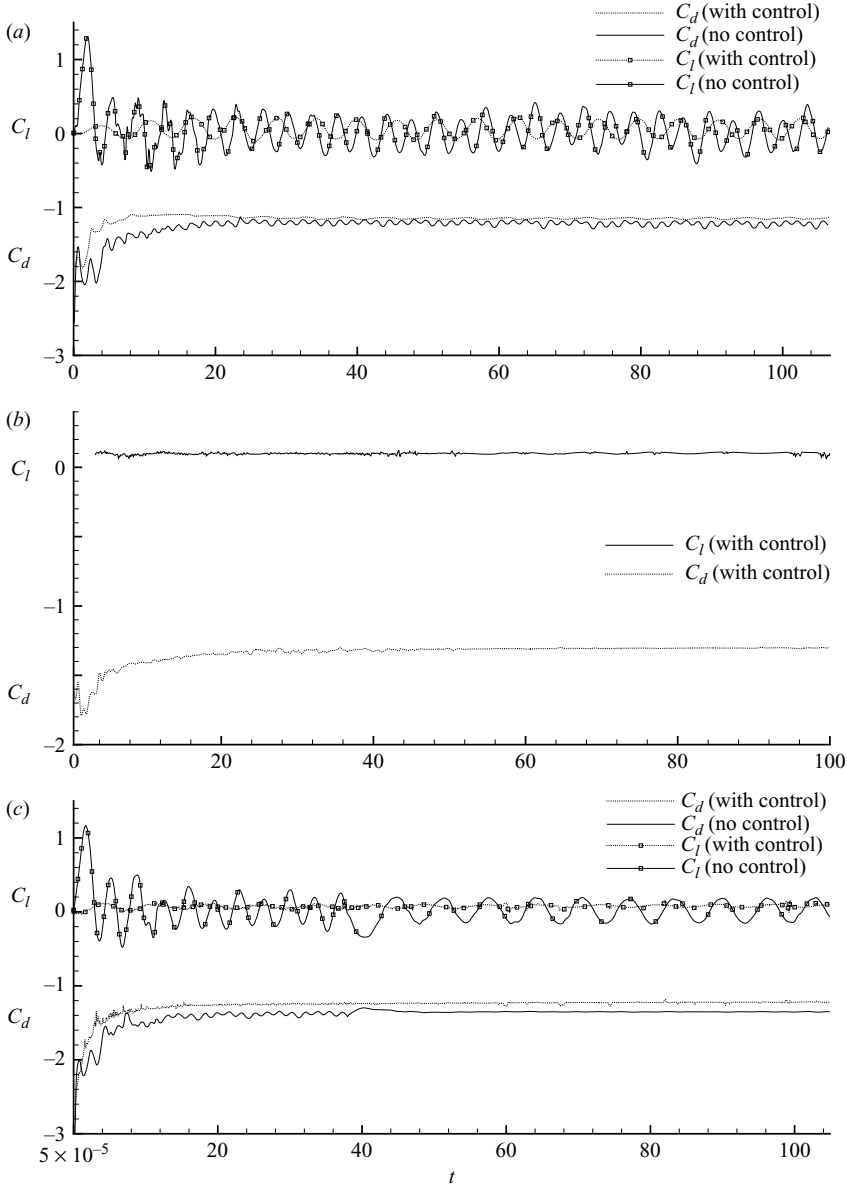


FIGURE 2. Variation of lift and drag coefficients with time for the cases indicated  
(a)  $Re = 150$ , (b) 63, (c) 79.

Q2

(1986) for  $Re = 80$ . For the uncontrolled case of  $Re = 79$ , our calculations provide  $F_R = 11.96$ , which compares with the experimental value of 13 (approx.) for  $Re = 80$ . Similarly, for the other computed cases, we have obtained the  $F_R$  and shown them in figure 3(a). The values show similar qualitative trends to those in figure 24 of Strykowski (1986). In figures 3(b) and 3(c), the power spectral density (PSD) of the computed  $C_l$  data are shown, plotted against the non-dimensional angular frequency. In these figures, the main peak is identified with the shedding frequency. The physical frequencies calculated using the PSD differ from the value calculated from the time-period value used in  $F_R$ . For  $Re = 63$ , this corresponds to  $f = 236.5$  Hz which is

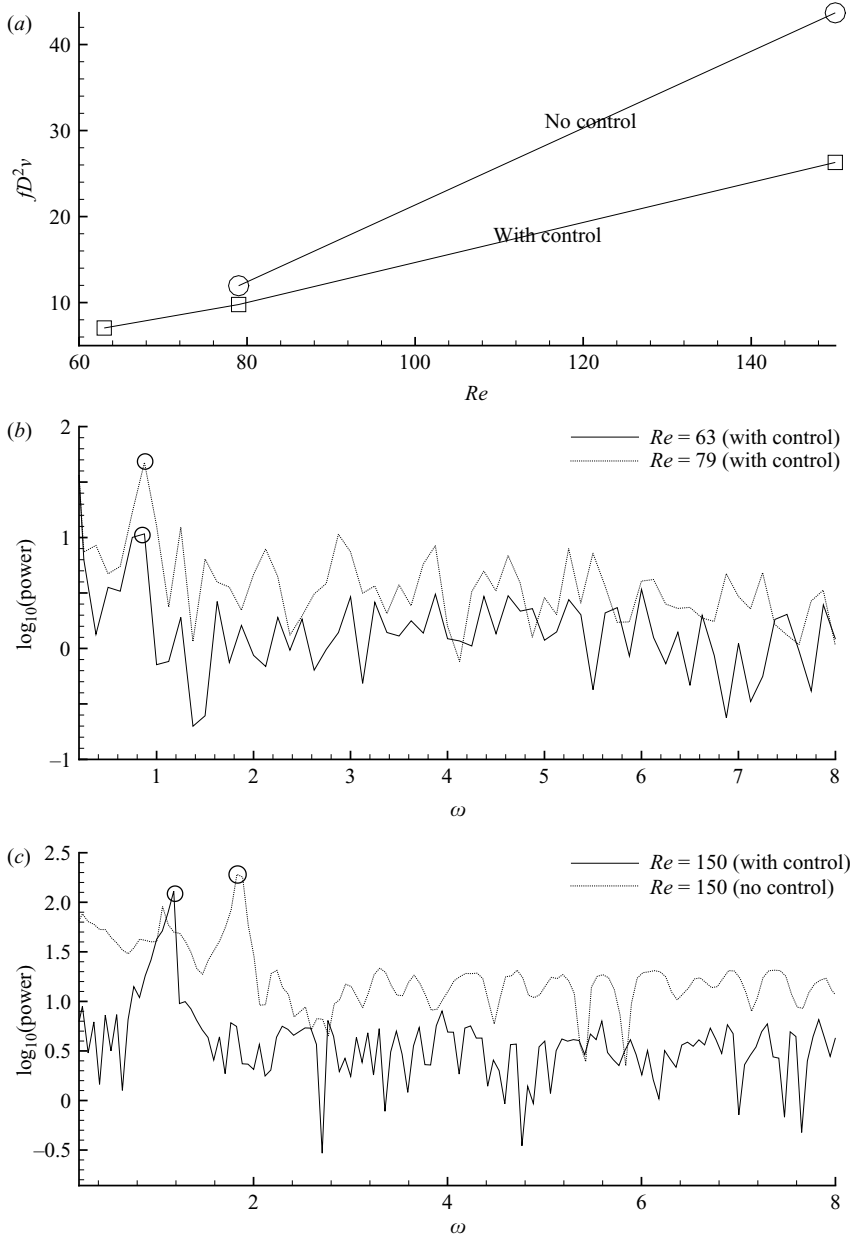


FIGURE 3. The Roshko numbers and power spectra shown for the indicated cases. In (b) and (c), the variable is non-dimensionalized angular frequency.

different from the value of 153.4 Hz obtained from  $F_R$ . A similar trend is noted for other Reynolds numbers as well. However, the values calculated from the Roshko number tend to match well with the experimental data. The calculated value of the shedding frequency from  $F_R$  is 212.76 Hz for the controlled case, as compared to 260.35 Hz for the uncontrolled case, for  $Re = 79$ . For  $Re = 150$ , the corresponding values of frequencies are 572 Hz and 950 Hz for controlled and uncontrolled cases, respectively. The calculated frequencies from  $F_R$  are similar to the results shown in figure 33 of Strykowski (1986).



Differences between the calculated and measured non-dimensional shedding frequencies can be understood if we look at the time scales and the time duration over which the experimental and computational data are acquired. For the experimental condition for  $Re = 63$  in the wind tunnel, the main cylinder used had a diameter of  $D = 0.083$  cm and the calculated free-stream speed is obtained as  $U_\infty = 1.518$  m s<sup>-1</sup>. In the computations, a convective time scale ( $D/U_\infty$ ) is used for non-dimensionalization, which works out as 0.000546 s. This implies that 1 s of physical experimentation is equivalent to calculating up to a non-dimensional unit of 1831.5. In the presented computations, a non-dimensional time step equal to 0.00005 has been used to perform near-neutral computations, while maintaining the DRP property. This small time step implies taking 36.63 million time steps used in computation to advance the physical time by 1 s. Thus, even computing up to 1 s following the impulsive start of the experiments is prohibitively expensive and time consuming. The results reported here are for up to a time when the flow has exhibited a few cycles of vortex shedding after the flow transient is gone. The experimental data have been collected over larger time intervals as compared to the computational data. However, the computational data has a far higher temporal resolution. All these must account for the difference in shedding frequency, in addition to the numerical errors and tolerances in the experiments.

Repeated measurements in Strykowski (1986) have revealed that the placement of a control cylinder causes the velocity defect to occur close to the cylinder axis, that is accompanied by a weak overshoot of the streamwise velocity profile over some width. In figure 4, the computed instantaneous streamwise velocity distribution at  $t = 70$  is shown as a function of  $y/D$  for all the cases either at  $x/D = 10$  or 20, that show such an overshoot. The experimental data were recorded at  $x/D = 58$ , which is far beyond our computational domain and could not be verified. However, we noted a reduction in the overshoot, when the velocity profile is farther downstream. The distinctive feature of a significantly reduced value of  $u$  at  $y/D = 0$ , for the controlled case as compared to the uncontrolled case is shown in figure 4(a) for  $Re = 79$ . Also, note that in figure 4, we have shown instantaneous velocity distribution, while that given in figure 20 of Strykowski (1986) corresponds to time-averaged velocity data. The overall agreement between the velocity distribution and shedding characteristics of experimental and computational results, shows the usefulness of the present computations, which can be exploited by undertaking detailed studies of the physics during such flow control, and this is performed next.

### 3. Vortex shedding as unsteady growth of disturbances

For the flow past an uncontrolled cylinder started impulsively, we see formation of symmetric recirculation regions at the base of the geometry immediately after the start. For Reynolds numbers greater than 500, we see secondary and tertiary vortices located symmetrically about the centreline. These wake bubbles grow in width and length while retaining symmetry up to a certain time, following which an asymmetry develops that leads to alternate growth of one of the bubbles that is shed, forming the Bénard–van Kármán street. In an experiment, this time of asymmetry is a function of Reynolds number and, in general, is facility dependent; Honji & Taneda (1969) report this non-dimensional time to be about 8 for  $Re = 200$ , whereas Coutanceau & Defaye (1991) report this non-dimensional time to be equal to 4 for  $Re = 10\,000$ . Hankey & Shang (1984) discuss the wake of bluff-body flows displaying two unstable modes – the stronger asymmetric mode defines the Strouhal number and the symmetric mode is

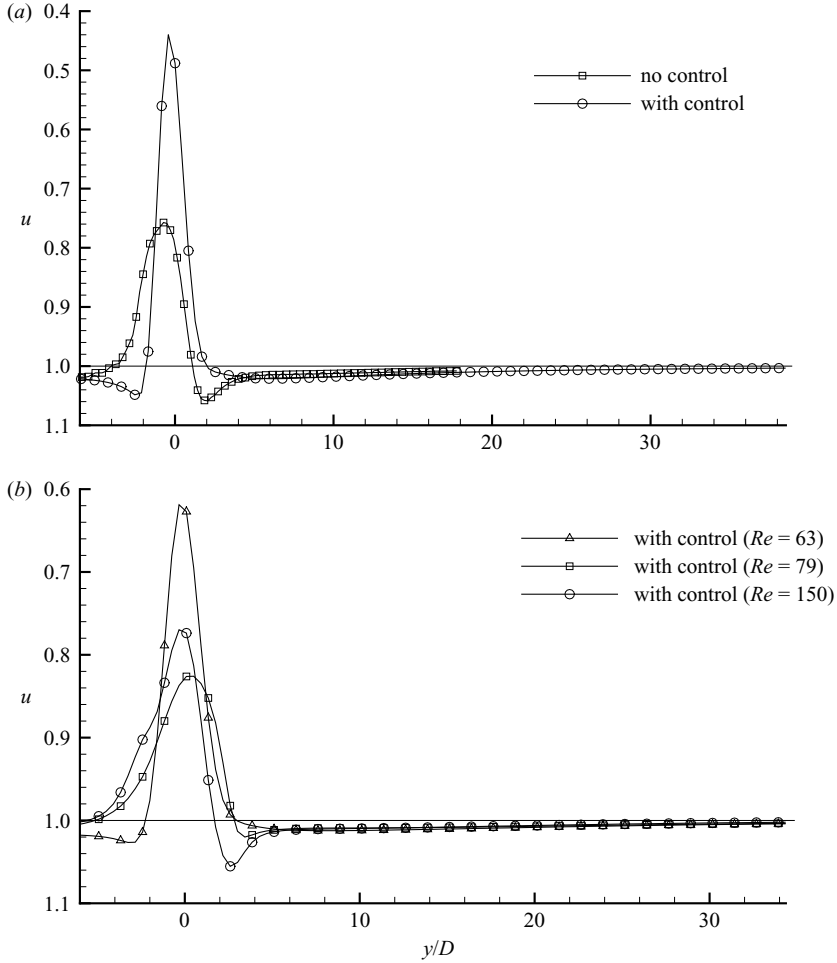


FIGURE 4. Instantaneous velocity distribution ( $t = 70$ ) at the indicated  $x/D$  locations for various cases: (a) For  $Re = 79$  controlled and uncontrolled cases are compared,  $x/D = 10$ ; (b) controlled cases compared for  $Re = 63, 79$  and  $150$ ,  $x/D = 20$ .

responsible for higher-frequency oscillation in the wake. Nair & Sengupta (1996) have shown that the computational onset of asymmetry is dependent upon the numerical method: the more accurate the method, the further delayed the onset of asymmetry will be. For low-accuracy methods (as in Braza, Chassaing & Ha Minh 1986), the onset of asymmetry is often suppressed and artificial means are used to trigger flow asymmetry. In the context of computations by the high-accuracy compact scheme, here, the control cylinder acts as a promoter of asymmetry in the wake of the main cylinder. This is evident from the  $C_l$  variation with time (figure 2).

In figure 5, streamline contour plots are shown over a single period, for different cases to show the effects of the control cylinder. For example, for  $Re = 79$ , figures 5(a) and 5(b) show the main effect is in the increased formation length of the bubbles in the near wake of the main cylinder. For the controlled case (figure 5a) the elongated bubbles change slowly with time. Compare this with the uncontrolled case (figure 5b). The presence of the control cylinder, essentially deflects and elongates the bubble and hence the flow becomes unsteady farther downstream, causing the shedding to be

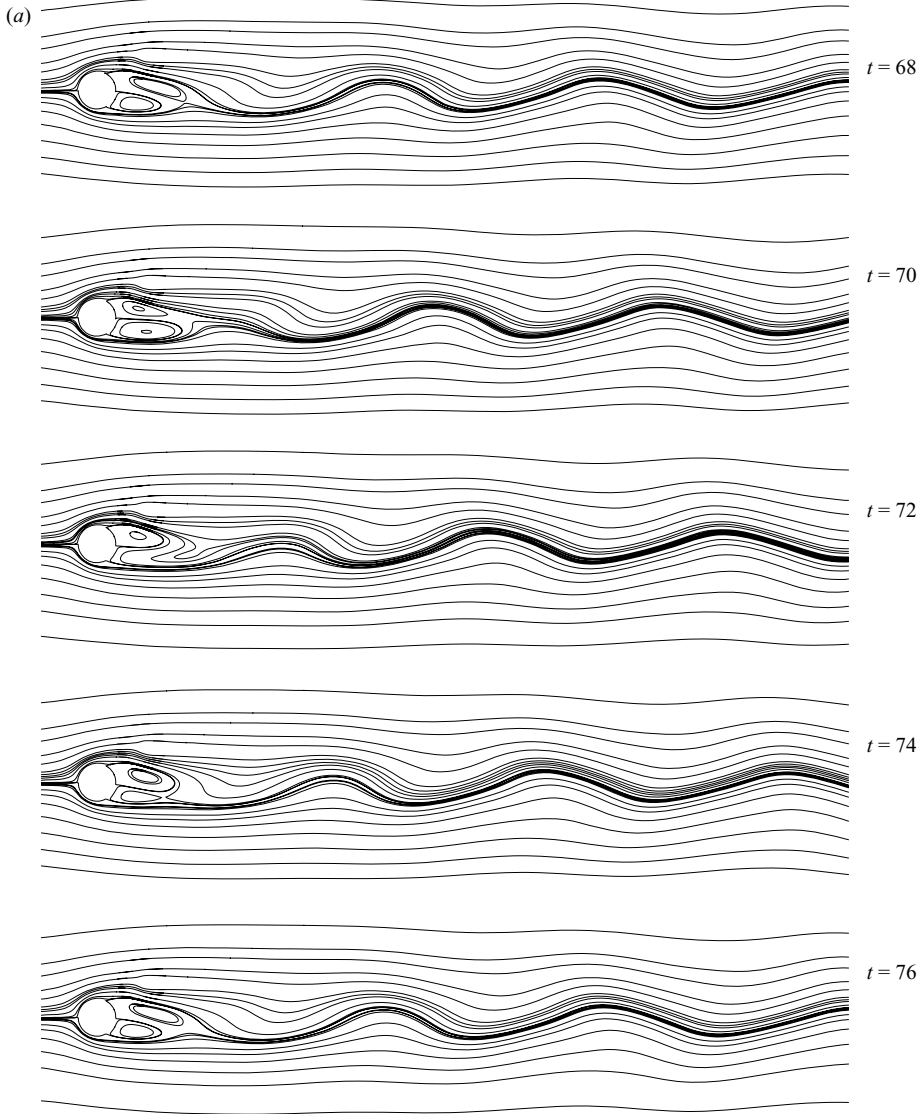


FIGURE 5. For legend see page 13.

weaker. The effects of the control cylinder can be seen better, for the case of  $Re = 63$ , (figure 5c). Because of the smaller value of the Reynolds number, the formation length is smaller, but the wake shows reduced unsteadiness and a distinct narrowing, as also shown in figure 17 of Strykowski (1986). Vorticity contour comparisons do not provide the same information, as shown here with the help of streamline contours, and further discussion on this aspect is provided in the online Appendix.

The onset of asymmetry for the flows at  $Re = 63$  and  $79$  is discussed in the following with the help of equation (1.1) which was introduced in Sengupta *et al.* (2003a) to explain unsteady disturbance growth in boundary layers. This equation was also used to explain the subcritical transition for the attachment line boundary layer in Sengupta & Dipankar (2005) for the leading-edge contamination problem. The main feature of (1.1) is its derivation from the Navier–Stokes equation without

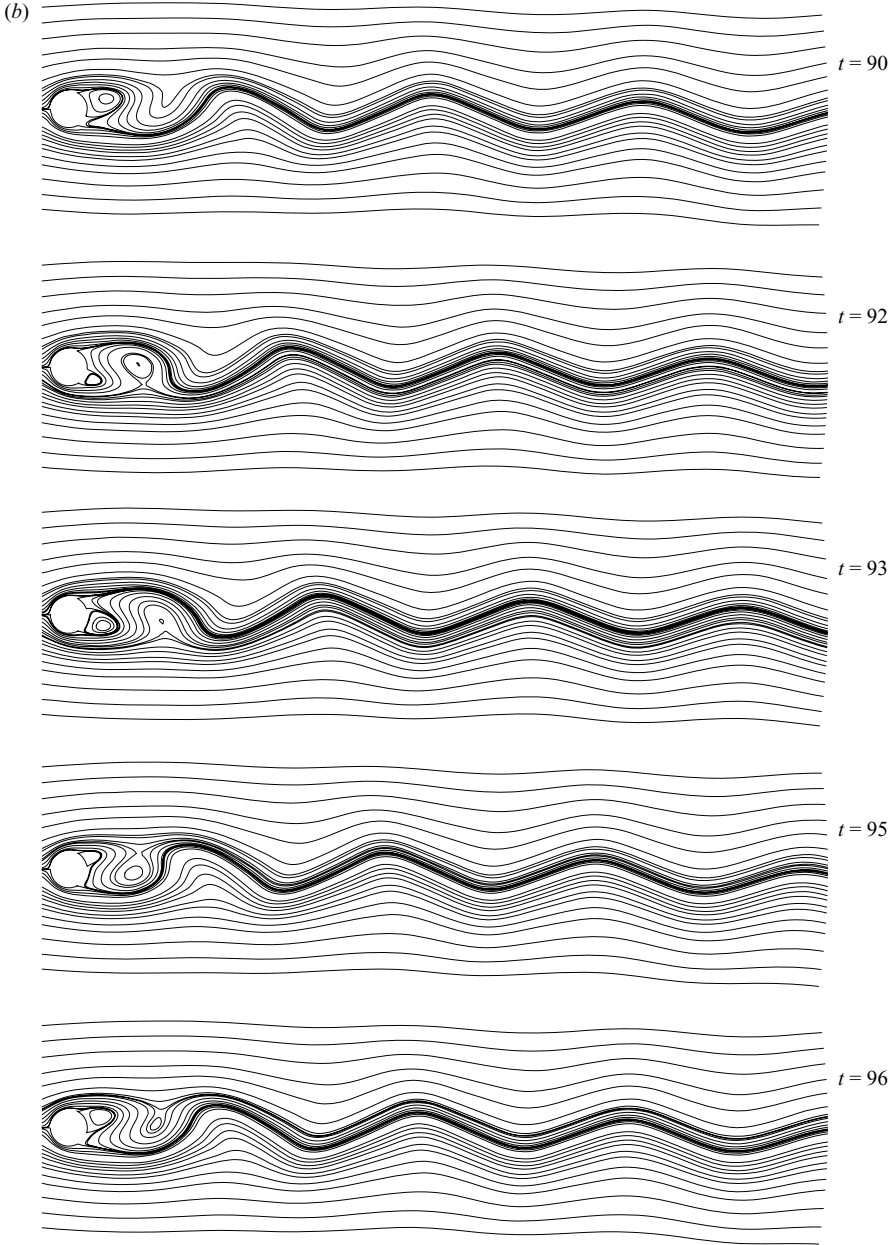


FIGURE 5. For legend see facing page.

any approximations, making it an ideal tool to study the spatio-temporal growth of disturbance energy for incompressible flow. We use (1.1) to study the onset of vortex shedding and its control, with the time average of the flow field for a single period. The time average over one period constitutes the equilibrium state, denoted by quantities with the subscript  $m$  on the right-hand side of equation (1.1). The instantaneous numerical solution of the Navier–Stokes equation provides the total solution, and thus, the disturbance quantities (indicated by the quantities with subscript  $d$ ) are obtained by subtracting the time average from the instantaneous field.

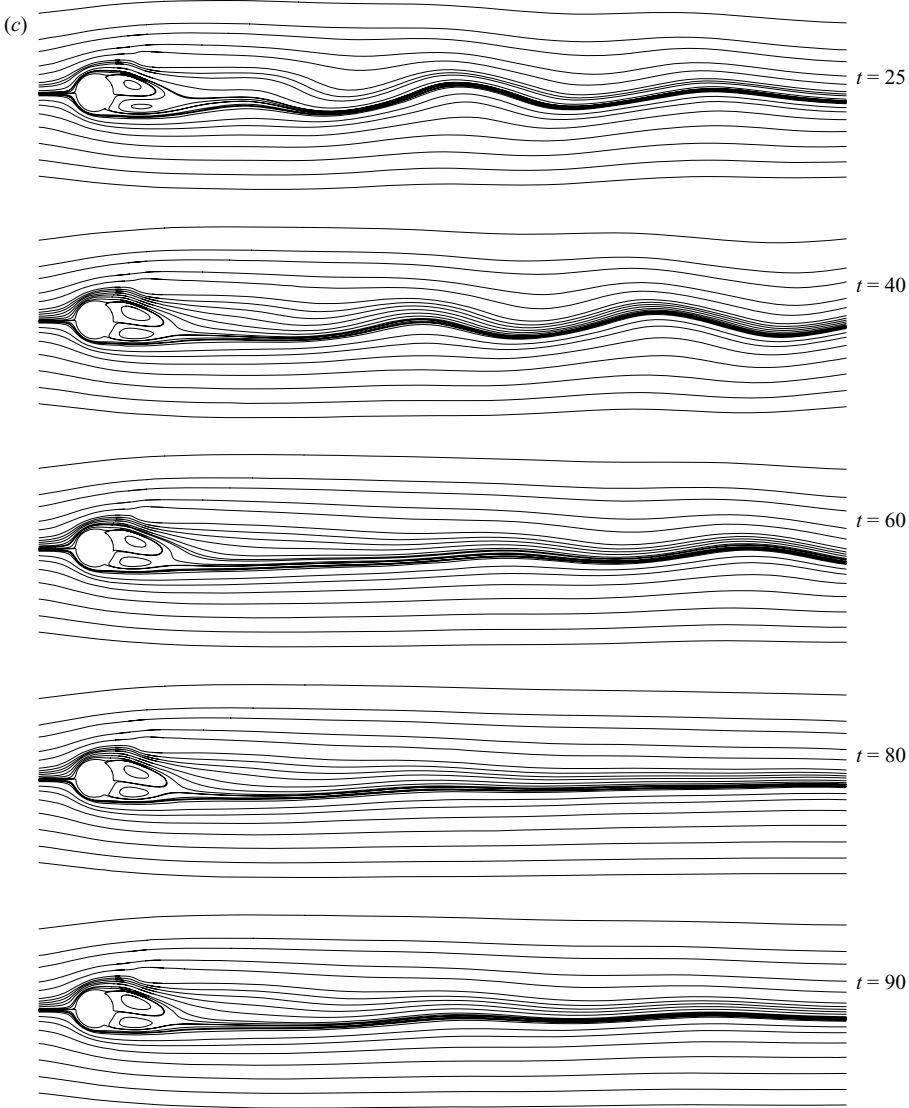


FIGURE 5. (a) Streamline contours for the controlled case for  $Re = 79$  during one approximate period of oscillation as seen in  $C_l$  vs. time plot. (b) Uncontrolled case for  $Re = 79$ . (c) Controlled case for  $Re = 63$ .

As in Sengupta *et al.* (2003a) and Sengupta & Dipankar (2005), equation (1.1) is not solved over the computational domain, instead the properties of the Poisson equation are used to identify disturbance energy source(s) and sink(s) in the domain by looking at the sign and magnitude of the right-hand side of the equation. A negative right-hand side at any place indicates the presence of a disturbance energy source locally, whereas a positive right-hand side represents a disturbance energy sink. These are shown by drawing the contour plots for  $Re = 79$ (figure 6a)(figure 6b) and 63. Negative contours are indicated by dotted lines shown during one cycle of oscillation at the indicated time instants. For both cases, the largest energy source(s) and sink(s) are associated with the control cylinder. Also, during the full cycle, these

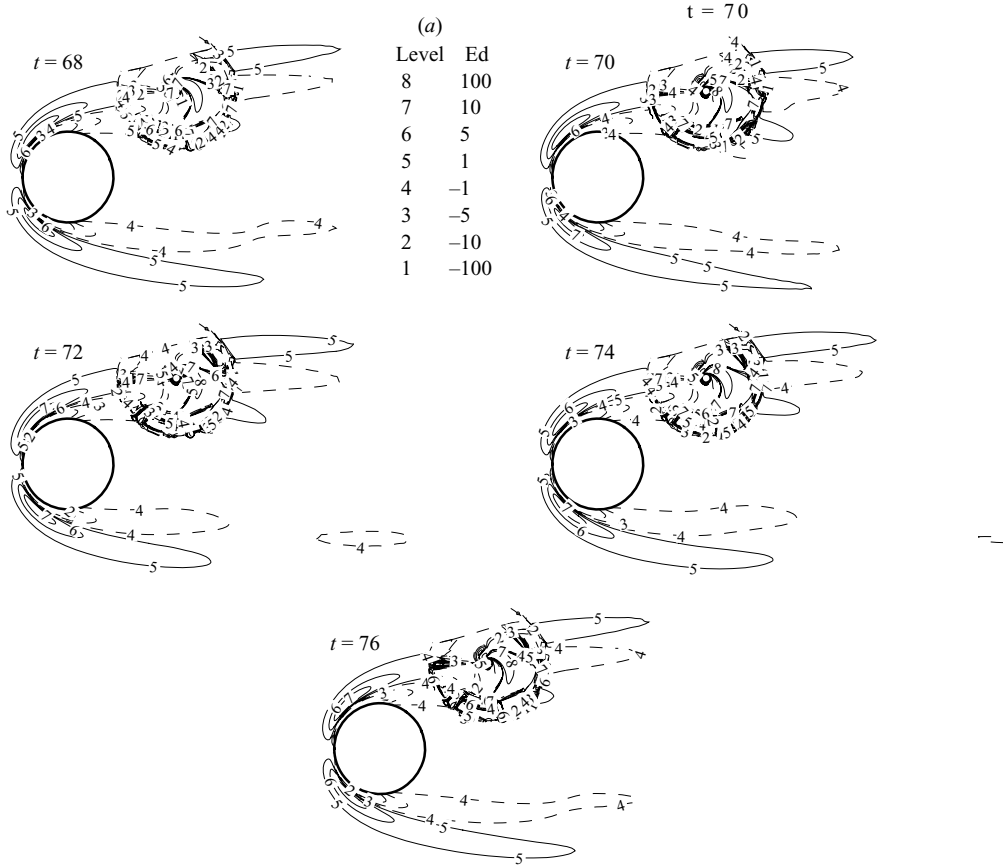


FIGURE 6. For legend see facing page.

source(s)/sink(s) change very slowly with time, indicating the effectiveness of the control. For the higher-Reynolds-number case, there is reduced shedding away from the main cylinder for the contour level, indicated by 4 in the figure. For the lower Reynolds number, even such weak shedding is not seen. Thus, the stabilizing effect is entirely due to the presence of the control cylinder. One reason for the difference of the flow field with Reynolds number is due to the difference of the equivalent Reynolds number for the control cylinder. Additionally, the oncoming shear flow over the control cylinder, will have significantly different effects at relatively low Reynolds numbers.

#### 4. Characterizing vortex shedding and control by POD

Shed vortices and their control can be attempted if we visualize them as coherent structures obtained from POD analysis following Sirovich (1987) and Holmes, Lumley & Berkooz (1996). For handling numerical data over a large domain by POD, the *method of snapshots* of Sirovich (1987) is most appropriate, in particular, if the number of input frames or *snapshots*,  $M$  is smaller than  $(N_x \times N_y)$ , the product of numbers of grid points along the coordinate directions.

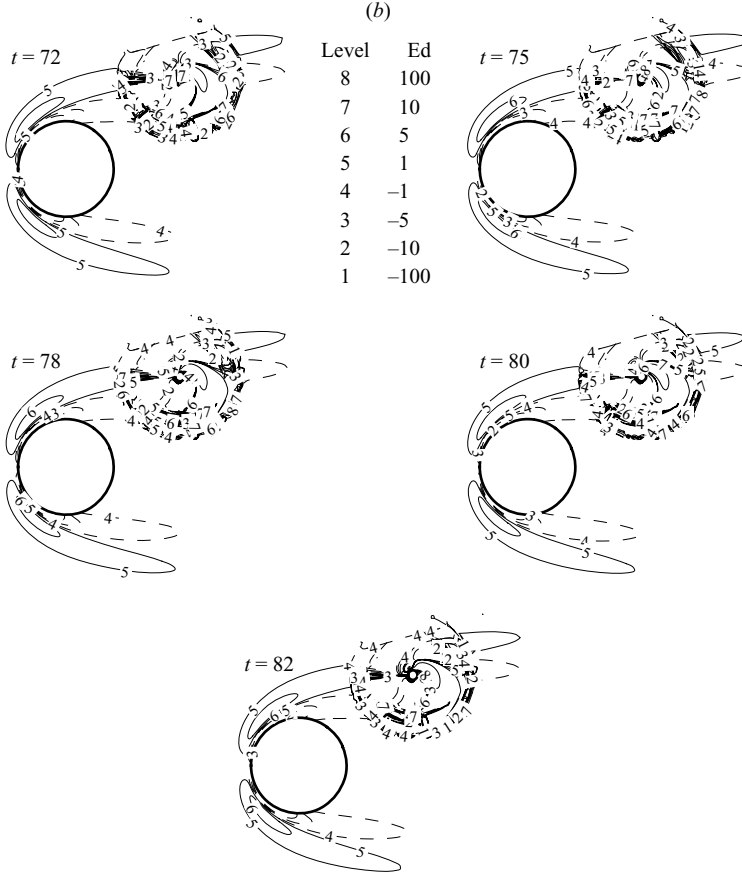


FIGURE 6. (a) Contours of the right-hand side of (1.1), for  $Re = 79$  controlled case. The dotted lines correspond to energy sources and solid lines represent sinks. The same contours, shown at  $t = 68$ , are used in all other frames. (b)  $Re = 63$ ,  $t = 72$ .

The data obtained by DNS provide the ensemble at  $M$  instants in time. If we define the time-varying part of the vorticity field as,

$$\omega'(x, t) = \sum_{m=1}^M a_m(t) \phi_m(x), \quad (4.1)$$

then the eigenvectors  $\phi_m$  are obtained as the eigenvectors of the covariance matrix whose elements are defined as  $R_{ij} = (1/M) \sum_{m=1}^M \omega'(x_i, t_m) \omega'(x_j, t_m)$  with  $i, j = 1, 2, \dots, N$  defined over all the collocation points totalling up to  $N$ . These complete eigenvectors have eigenvalues that give the probability of their occurrence and their sum giving the total enstrophy of the system. The time dependence obtained from the Galerkin expansion of the flow field cannot be used to study absolute instability of the near wake, as POD is a statistical projection of the disturbance field with respect to an appropriately chosen mean field.

In table 1, the first few leading eigenvalues for different computed cases are shown, which were obtained by taking forty snapshots. To produce a correct statistical picture, it is necessary to remove the effects of early transients. In figure 7, results of two

Serial number	Eigenvalues ( $Re = 63$ , controlled)	Eigenvalues ( $Re = 79$ , controlled)	Eigenvalues ( $Re = 79$ , uncontrolled)	Eigenvalues ( $Re = 150$ , controlled)	Eigenvalues ( $Re = 150$ , uncontrolled)
1	0.5564598	2.3509881	4.2289697	9.1175491	21.7850086
2	0.5261365	2.2717989	4.1153238	7.9681241	8.5146694
3	0.0933332	0.2374371	0.4863833	1.5971635	3.4299210
4	0.0620794	0.2268858	0.4740239	1.5190875	3.1781699
5	0.0473023	0.0581371	0.3172718	0.5037713	1.2976231
6	0.0397634	0.0459855	0.2865087	0.4175717	1.1960167
7	0.0377989	0.0389407	0.1683907	0.3374339	0.6433015
8	0.0087726	0.0374733	0.1495850	0.3209011	0.5159717
9	0.0058059	0.0272480	0.1224876	0.2700002	0.4200889
10	0.00510475	0.0091951	0.0950606	0.1997370	0.3506392

TABLE 1. Leading eigenvalues for various cases.

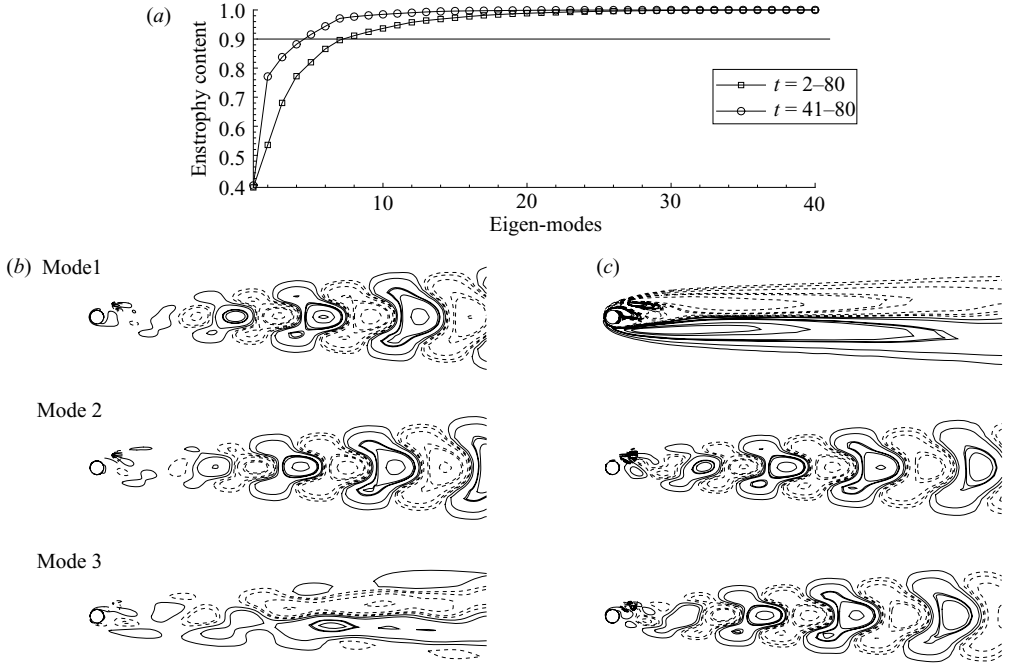


FIGURE 7. POD analysis for  $Re = 63$  controlled case with: (a) cumulative enstrophy distribution among the eigen-modes using full data from  $t = 2$  to 80 and from  $t = 41$  to 80, to show the effects of early transients; (b) eigenfunctions for the case without transient ( $t = 41-80$ ) and (c) eigenfunctions for the case with transient effects ( $t = 2-80$ ).

cases for  $Re = 63$  are compared, with one set produced by taking data from  $t = 2$  to 80, the other from  $t = 41$  to 80. In figure 7(a), the cumulative enstrophy contents are compared for the two cases, while the corresponding first three eigen-modes are shown in figures 7(b) and 7(c). Removal of the early transients has a significant effect on the PODs, requiring far fewer modes to represent the same amount of enstrophy of the



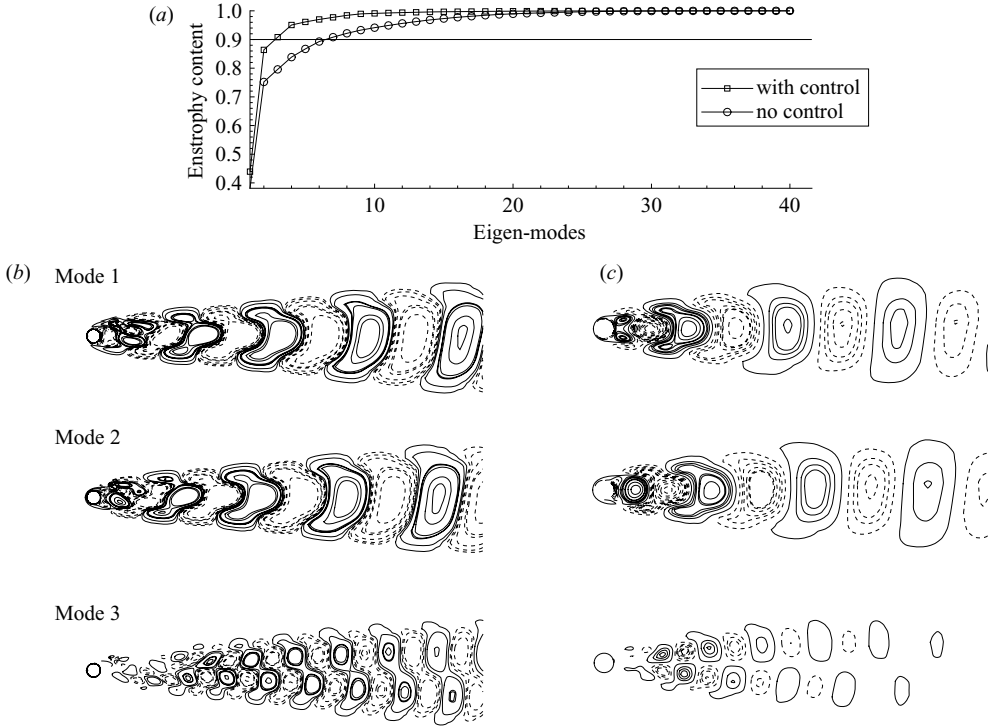


FIGURE 8. POD analysis for  $Re = 79$  case, with and without control: (a) cumulative enstrophy distribution among the eigen-modes using full data from  $t = 41$  to 80; (b) eigenfunctions for the controlled case and (c) eigenfunctions for the uncontrolled case.

flow field. Thus, the remaining PODs shown here would correspond to data sets after removal of the early transient effects, which can be used for a possible low-dimensional description of vortex shedding, as most of the energy/enstrophy are contained in the first few modes only. There is a definitive pattern for the eigenvalues with changes in Reynolds number for the controlled and uncontrolled cases. Reduction of Reynolds number or introduction of control reduces the eigenvalues monotonically for all the modes.

In figures 8 and 9, we have compared the PODs between the controlled and uncontrolled cases for  $Re = 79$  and 150, respectively. For the controlled cases, the first two modes account for more than 75 % of the enstrophy. Thus, control brings in coherence in the wake vortical structures. The alternate signed arrowhead structures, for the first two eigenmodes, are the building blocks for the vorticity distribution. Vortex shedding begins from where these structures originate. When two modes carry most of the enstrophy, the pattern of vortex shedding is determined by the phase shift between these two. It is noted in Deane *et al.* (1991) and Deane & Mavriplis (1994) that the travelling characteristic (during the transformation from absolute to convective instability) of the vortex street is due to the coupling of a pair of similar amplitude modes that are out of phase by a quarter of a period. In general, higher modes are antisymmetric about the wake centreline. For controlled cases, this antisymmetry is seen to be prominent, although the enstrophy carried in the controlled case is lower as compared to the uncontrolled case.

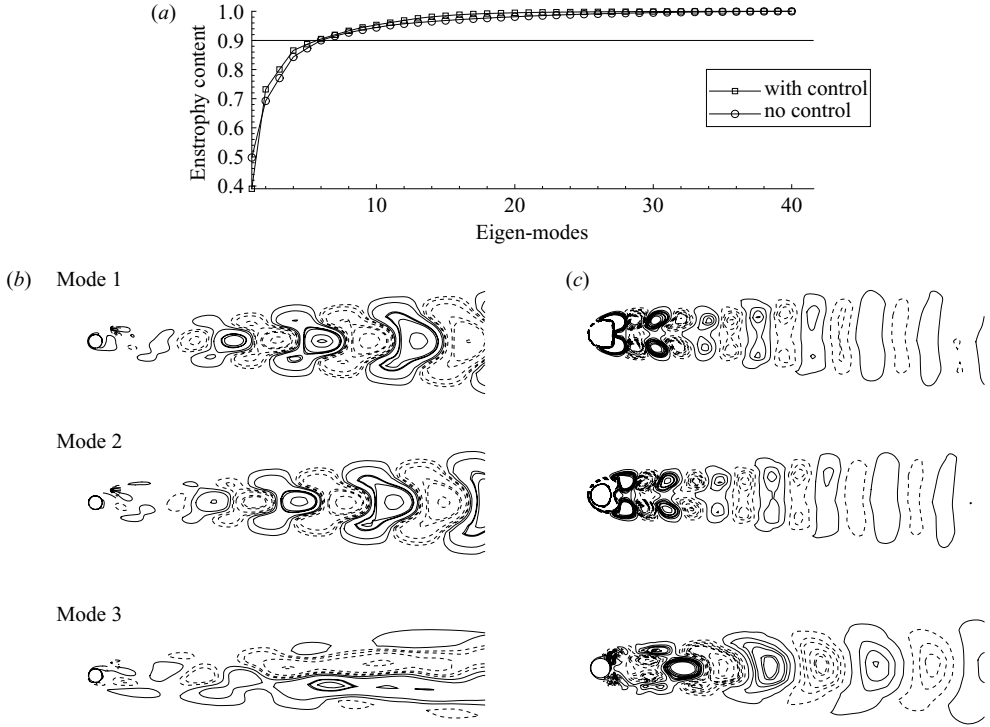


FIGURE 9. POD analysis for  $Re=150$  case, with and without control: (a) cumulative enstrophy distribution among the eigen-modes using full data from  $t=41$  to 80; (b) eigenfunctions for the controlled case and (c) eigenfunctions for the uncontrolled case.

## 5. Summary

Results from a numerical study are reported here for the alteration of the vortex-shedding pattern in the wake of a cylinder at low Reynolds numbers (63, 79 and 150), by placing a smaller control cylinder in the near wake of the main cylinder. Numerical results have been obtained by using a high spectral accuracy compact scheme employing an over-set grid method developed for this work. Detailed numerical properties of various schemes to capture the present flow field are given in the online Appendix, to explain why the present method is successful. Computed results have been validated by comparing them with the experimental results reported in Strykowski (1986) and Strykowski & Sreenivasan (1990) for  $Re=63$  and 79. For all the Reynolds-number cases, placement of the control cylinder leads to the following effects: (i) suppression of vortex shedding, in terms of reduced amplitude of unsteady variation for lift which also leads to narrowing of the wake; (ii) decreased shedding frequency; and (iii) drag reduction. The suppression of vortex shedding and reduction of drag can be seen from the time variation of  $C_l$  and  $C_d$  shown in figure 2. Suppression and alteration of the shedding pattern can be seen figure 3, which shows the variation of the Roshko number and the power spectral density with and without the control cylinder. For example, from figures 3(b) and 3(c), we see that the shedding frequency reduces on the introduction of the control cylinder, which matches the experimental results given in Strykowski (1986). Instantaneous velocity distribution in the wake of the cylinder (figure 4) also shows qualitative agreement with similar figure shown in Strykowski (1986).

The reason behind the flow control achieved via the introduction of the control cylinder is explained through the flow structure shown with the streamfunction contour plots of figure 5. For the flow without control, the formation length is short and we see significant normal oscillation of the wake immediately behind the main cylinder (figure 5b). On the introduction of the control cylinder, this normal oscillation is suppressed, which leads to the formation of a quasi-symmetric attached deflected bubble in the near wake. Delayed normal oscillation also leads to longer formation length and narrower wake-width. The latter, in turn, leads to drag reduction (figure 5a). At this Reynolds number, the wake oscillation is seen to occur at a station farther downstream. For  $Re = 63$ , the quasi-symmetric near-wake bubble is comparatively shorter, but the reduced Reynolds number displays completely suppressed wake oscillation and a significant narrowing of the far wake.

The effect of the control cylinder is also explained by using the receptivity equation (1.1) developed in Sengupta *et al.* (2003a) to explain bypass transition. Application of the same for the present case in figure 6, shows that the control cylinder is responsible for creating different effects at different Reynolds numbers. This is because the effective Reynolds number for the control cylinder is small, but has different diffusive effects for the cases considered (6.3 for  $Re = 63$  to 21.4 for  $Re = 150$ ). Also, the effects of shear of the oncoming flow at such lower Reynolds numbers over the control cylinder contributes to the difference. As seen in these figures, the control cylinder acts as the disturbance energy sink affecting the normal cycle of vortex shedding.

The direct simulation data are also analysed using the POD technique of Holmes *et al.* (1996) and Sirovich (1987) in figures 7 to 9, to explain the function of the control cylinder. It is seen that the presence of the arrowhead structures of the leading eigenmodes are the building blocks for vortical distribution in the wake. Linear superposition and pairwise coupling of these are responsible for alternate vortical shedding in uncontrolled flows. The introduced control cylinders focus total energy/enstrophy on fewer eigenmodes. The higher modes (that are also antisymmetric) carry very little energy/enstrophy of the flow and are not significant. Also, the presence of the control cylinder has the effect of narrowing the wake in comparison to the uncontrolled case (figures 8 and 9).

## REFERENCES

- BRAZA, M., CHASSAING, P. & HA MINH, H. 1986 Numerical study and physical analysis of the pressure and velocity fields in the near wake of a circular cylinder. *J. Fluid Mech.* **165**, 79–130.
- CHESSHIRE, G. & HENSHAW, W. D. 1990 Composite overlapping meshes for the solution of partial differential equations. *J. Comput. Phys.* **90**, 1–64.
- COUTANCEAU, M. & DEFAYE, J. R. 1991 Circular cylinder wake configuration: a flow visualization survey. *Appl. Mech. Rev.* **44**, 225–305.
- DEANE, A. E. & MAVRIPLIS, C. 1994 Low-dimensional description of the dynamics in separated flow past thick airfoils. *AIAA J.* **32**, 1222–1227.
- DEANE, A. E., KEVREKIDIS, I. G., KARNIADAKIS, G. E. & ORSZAG, S. A. 1991 Low-dimensional models for complex geometry flows: application to grooved channels and circular cylinders. *Phys. Fluids A* **3**, 2337–2354.
- ESPOSITO, P. G., VERZICCO, R. & ORLANDI, P. 1993 Boundary condition influence on the flow around a circular cylinder. In the *Proc. IUTAM Symp. on Bluff-body Wakes, Dynamics and Instabilities* (ed. E. Eckelmann, G. Graham, P. Huerre & P. A. Monkewitz). Springer.
- HANKEY, W. L. & SHANG, J. S. 1984 Numerical simulation of self-excited oscillations in fluid flows. In *Computational Methods in Viscous Flows* (ed. W. G. Habashi), vol. 3. Pineridge, Swansea.
- HENSHAW, W. D. 1994 A fourth order accurate method for the incompressible Navier–Stokes equations on overlapping grids. *J. Comput. Phys.* **113**, 13–25.

- HOLMES, P., LUMLEY, J. L. & BERKOOZ, G. 1996 *Turbulence, Coherent Structures, Dynamical Systems and Symmetry*. Cambridge University Press.
- HONJI, H. & TANEDA, S. 1969 Unsteady flow past a circular cylinder. *J. Phys. Soc. Japan* **27**, 1668–1677.
- JACKSON, C. P. 1987 A finite element study of the onset of vortex shedding in flow past variously shaped bodies. *J. Fluid Mech.* **182**, 23–45.
- NAIR, M. T. & SENGUPTA, T. K. 1996 Onset of asymmetry: flow past circular and elliptic cylinders. *Intl J. Numer. Meth. Fluids* **23**, 1327–1345.
- ORLANDSKI, I. 1976 A simple boundary condition for unbounded hyperbolic flows. *J. Comput. Phys.* **21**, 251–259.
- SENGUPTA, T. K. 2004 *Fundamentals of Computational Fluid Dynamics*. Universities Press, Hyderabad, India.
- SENGUPTA, T. K. & DIPANKAR, A. 2005 Subcritical instability on the attachment-line of an infinite swept wing. *J. Fluid Mech.* **529**, 147–171.
- SENGUPTA, T. K., DE, S. & SARKAR, S. 2003a Vortex-induced instability of an incompressible wall-bounded shear layer. *J. Fluid Mech.* **493**, 277–286.
- SENGUPTA, T. K., GANERIWAL, G. & DE, S. 2003b Analysis of central and upwind compact schemes. *J. Comput. Phys.* **192**, 677–694.
- SENGUPTA, T. K., KASLIWAL, A., DE, S. & NAIR, M. 2003c Temporal flow instability for Magnus–Robins effect at high rotation rates. *J. Fluids Struct.* **17**, 941–953.
- SENGUPTA, T. K., TALLA, S. B. & PRADHAN, S. C. 2005 Galerkin finite element methods for wave problems. *Sadhana* **30**, 611–623.
- SENGUPTA, T. K., VIKAS, V. & JOHRI, A. 2006 An improved method for calculating flow past flapping and hovering airfoils. *Theoret. Comput. Fluid Dyn.* **19**, 417–440.
- SIROVICH, S. 1987 Turbulence and the dynamics of coherent structures. Parts I, II and III. *Q. Appl. Maths* **45**, 561–590.
- SREENIVASAN, K. R., STRYKOWSKI, P. J. & OLINGER, D. J. 1987 Hopf bifurcation, Landau equation and vortex ‘shedding’ behind circular cylinders. In *Forum on Unsteady Flow Separation* (ed. K. N. Ghia), pp. 1–13. ASME.
- STEGER, J. L. & BENEK, J. A. 1987 On the use of composite grid schemes in computational aerodynamics. *Comput. Meth. Appl. Mech. Engng* **64**, 301–320.
- STRYKOWSKI, P. J. 1986 The control of absolutely and convectively unstable shear flows. PhD dissertation, Yale University.
- STRYKOWSKI, P. J. & SREENIVASAN, K. R. 1990 On the formation and suppression of vortex ‘shedding’ at low Reynolds numbers. *J. Fluid Mech.* **218**, 74–107.